



UNIVERSIDADE ESTADUAL DE CAMPINAS SISTEMA DE BIBLIOTECAS DA UNICAMP REPOSITÓRIO DA PRODUÇÃO CIENTIFICA E INTELECTUAL DA UNICAMP

Versão do arquivo anexado / Version of attached file:

Versão do Editor / Published Version

Mais informações no site da editora / Further information on publisher's website:

https://pubs.rsc.org/en/content/articlelanding/2021/CP/D0CP05891B

DOI: 10.1039/D0CP05891B

Direitos autorais / Publisher's copyright statement:

©2021 by Royal Society of Chemistry. All rights reserved.

PCCP



PAPER



Cite this: Phys. Chem. Chem. Phys., 2021, 23, 3019

Received 11th November 2020 Accepted 23rd December 2020

DOI: 10.1039/d0cp05891b

rsc.li/pccp

Inverse halogen dependence in anion ¹³C NMR†

Renan V. Viesser * and Cláudio F. Tormena * *

Halogens cause pronounced and systematic effects on the 13 C NMR chemical shift (δ^{13} C) of an adjacent carbon nucleus, usually leading to a decrease in the values across the halogen series. Although this normal halogen dependence (NHD) is known in organic and inorganic compounds containing the carbon atom in its neutral and cationic forms, information about carbanions is scarce. To understand how δ^{13} C changes in molecules with different charges, the shielding mechanisms of CHX₃, CX₃⁺, and CX_3^- (X = Cl, Br, or I) systems are investigated via density functional theory calculations and further analyzed by decomposition into contributions of natural localized molecular orbitals. An inverse halogen dependence (IHD) is determined for the anion series as a result of the negative spin-orbit contribution instead of scalar paramagnetic effects. The presence of a carbon nonbonding orbital in anions allows magnetic couplings that generate a deshielding effect on the nucleus and contradicts the classical association between δ^{13} C and atomic charge.

Introduction

NMR chemical shift (δ) , being one of the most reliable tools in determining molecular structures, is a valuable source of electronic density information surrounding the nucleus. 1-7 However, the applications of δ go beyond the molecular assignment. The high sensitivity of δ to the chemical environment experienced by the nucleus is frequently used as a probe to study different aspects of chemical bonding.8,9 Relevant insights in crystallography, 10,11 intra- and intermolecular interactions, 12-14 catalytic processes, 15,16 and molecular reactivity 17,18 have increasingly expanded the applications of δ .

The magnetic effect of the electronic structure on the nucleus, induced by the application of an external magnetic field (B_0) , is more fundamentally described by the shielding constant (σ) . ¹⁹ The difference between σ for a nuclear isotope in a reference compound (ref) and a probe environment corresponds to δ measured in the solution NMR spectrum (eqn (1)). When the reference shielding becomes very large, the expression must be divided by $(1 - \sigma_{ref})$:

$$\delta = \frac{\sigma_{\rm ref} - \sigma}{1 - \sigma_{\rm ref}} \approx \sigma_{\rm ref} - \sigma \tag{1}$$

Thus, a positive shielding corresponds to smaller δ values, whereas a deshielding or negative shielding is associated with larger δ ones.

Institute of Chemistry, University of Campinas - UNICAMP, P.O. Box 6154, 13083-970, Campinas, São Paulo, Brazil. E-mail: renan.viesser@gmail.com, tormena@unicamp.br

† Electronic supplementary information (ESI) available. See DOI: 10.1039/

Here, σ is an anisotropic property that depends on the magnitude of the local field generated by the electrons, as well as the orientation of the molecule with B_0 . Therefore, σ is represented by a second-rank tensor containing three principal orthogonal components (σ_{11} , σ_{22} , and σ_{33}).^{20,21} A detailed analysis of the anisotropic character of σ , *i.e.*, a comprehensive investigation about the magnitude, sign, and orientation of the principal components relative to the molecular coordinate frame, enables the understanding of shielding mechanisms.^{22,23} The electronic origin of these mechanisms is interpreted computationally by splitting each principal component into diamagnetic (σ^{dia}), paramagnetic (σ^{para}), and spinorbit (σ^{SO}) contributions. 24,25

The diamagnetic term arises from small magnetic fields generated by the circulation of electrons which oppose the applied B_0 leading to shielding of the nucleus. They originate from the electronic density at the ground state of the molecule and come mostly from core electrons. 9,21,24

The interpretation of σ^{para} is considerably more complex than that of σ^{dia} because the former is generated by the mixing of occupied and vacant orbitals. 24 The presence of B_0 induces paramagnetic currents on the nucleus through couplings between occupied and vacant orbitals perpendicular to each other upon the action of component i of the angular momentum operator (\hat{L}_i) . The magnitude of σ^{para} along direction i is proportional to the overlap between coupled orbitals and inversely proportional to the energy gap between them (Fig. 1). Moreover, σ^{para} is more pronounced if the orbitals are polarized toward the nucleus of interest because the \hat{L}_i operator is weighted by the inverse cube of the electronnucleus distance. 21,24-26 Couplings between perpendicular

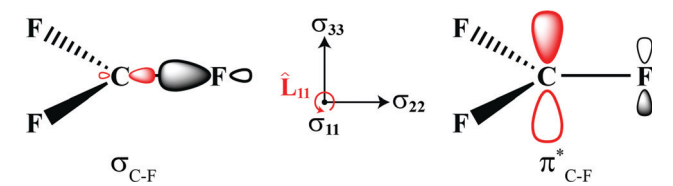


Fig. 1 Representation of occupied σ_{C-F} and unoccupied π^*_{C-F} orbitals that magnetically couple upon the action of the angular momentum operator, resulting in deshielding along direction 11 of the $\mathsf{CF_3}^+$ molecule.

occupied orbitals could also generate paramagnetic currents on the nucleus, but the magnitude tends to be smaller. 24

Paramagnetic contributions usually lead to nuclear deshielding (negative values) and are strongly affected by the chemical environment. The effect of symmetry and orbital energy on σ^{para} is the main reason for the anisotropy of σ and can provide insights about frontier orbitals and molecular reactivity. ^{16–18,21,27,28}

In a non-relativistic limit, only diamagnetic and paramagnetic mechanisms add up to σ . However, the spin–orbit term contributes significantly to σ when relativistic effects are present, *i.e.*, there is at least one heavy atom (HA) in the molecule. One of the most well-known relativistic effects on σ is the HALA, in which the nuclear shielding of a light atom (LA), such as 1 H or 13 C, undergoes pronounced effects when it is located near a HA. 9,29,30

The HALA effect usually occurs due to spin polarization at the HA caused by the spin–orbit (SO) coupling. In the presence of B_0 , SO coupling generates a non-zero spin density at the HA that propagates to the neighboring LA through the Fermicontact (FC) mechanism. SO contributions to the σ of the LA show a strong dependence on the HA nuclear charge ($\sim Z^2$) and can be either positive (nuclear shielding) or negative (nuclear deshielding). The sign of $\sigma^{\rm SO}$ depends on the occupation and symmetry of the frontier orbitals involved in the SO/FC transmission, especially when nonbonding orbitals or lone pairs (LPs) of the HA are available. $^{29-33}$

Many other electronic factors have been demonstrated to influence the efficiency of SO/FC transmission, mainly concerning the character of the HA–LA bond. For instance, $\sigma^{\rm SO}$ tends to be more pronounced if the valence orbitals of the LA show a higher s-character and the energy gap between occupied and vacant orbitals is smaller. 30,32,34 For a complete understanding of the intensity and sign of magnetic couplings to the SO/FC mechanism, we suggest reading recent papers from Vícha and co-authors. 29,34

Among the several HALA effects reported in the literature, the halogen one shows a high magnitude and systematic variations in the δ of the LA. The δ of the LA displays typically one of the two trends in going from F to Cl to Br to I substituents: normal halogen dependence (NHD) or inverse halogen dependence (IHD). The first one refers to a decrease in the δ of the LA across the halogen series, *i.e.*, the LA nucleus is increasingly shielding with increase in the halogen atomic number (Z_X). NHD is mainly caused by the SO coupling. In contrast, IHD corresponds to the reverse deshielding trend of

the LA and tends to arise from the paramagnetic contributions that overcome the SO ones in some halides of early transition metals or main group elements in low oxidation states. 32,35,36

The effects of halogens on the $\delta^{13}\mathrm{C}$ are observed easily due to the carbon nucleus being highly sensitive to the presence of the HA, especially in a one-bond distance. To the best of our knowledge, only NHD was reported for the carbon nucleus because the SO contribution from halogens generates a shielding effect ($\sigma^{\mathrm{SO}}>0$) on the $\sigma^{13}\mathrm{C}$. However, SO contributions to the $\sigma^{13}\mathrm{C}$ can be negative for other HAs. For example, Rusakov et al. The investigated the behavior of negative SO coupling in the 13th and 14th groups of the Periodic Table, the inverse trends of which on the $\sigma^{13}\mathrm{C}$ (similar to IHD) were named triel and tetrel dependence, respectively.

Although the HALA effect on the σ^{13} C is well-documented, most of the articles focus on molecules containing carbon atoms in neutral and cationic forms. Studies on δ^{13} C for carbanions are limited $^{38-41}$ mainly due to the short-lived nature of these species in the condensed phase, which makes it difficult to acquire experimental values. It is known that neutral and cationic carbons undergo NHD across the halogen series; $^{42-51}$ however, no information regarding carbanions was found by us. HALA effects on carbanions like CX $_3$ are intriguing because non-linear trends are observed for similar systems, such as PX $_3$. The PX $_3$ shows an intermediate behavior between NHD and IHD, and the δ^{31} P increases from F to Br before dropping slightly to I. 52

In addition to the reasons mentioned above, the particular choice of anions has been motivated by the recent experimental and theoretical ^{13}C NMR characterization of $\text{CF}_3^{-.53}$ The larger $\delta^{13}\text{C}$ of the anion (175.0 ppm) in comparison to neutral (CHF3, 122.2 ppm) and cationic (CF3+, 150.7 ppm) derivatives was explained, in our recent publication, 40 as a result of strong paramagnetic couplings involving the carbon lone pair. It is interesting to investigate how the energy gap between occupied and vacant orbitals, halogen electronegativity, and the halogen orbital size affect the σ of carbanions by expanding the previous study to the remaining halogens.

To fill this gap of knowledge, CX_3^- (X = Cl, Br, or I), since fluorine derivatives were recently published, 40 molecules were selected for the present computational work, as well as the NHD of CHX_3 and CX_3^+ were revisited. This study aims to provide a guideline to understand the shielding mechanisms for three cases of carbon electronic structure using Kohn–Sham density functional theory (KS-DFT). In short, we provide an intuitive picture of the shielding mechanisms for the three systems, showing how the connection between σ and the electronic structure goes beyond the simplistic explanation based on electronic charge.

Experimental details

The 13 C NMR spectra of CHX₃ (X = Cl, Br, or I) were recorded using a Bruker Avance III spectrometer operating at 499.87 MHz and 125.69 MHz for 1 H and 13 C, respectively. Measurements

were carried out using a 5 mm Smart probe, at a nominal temperature of 25 °C, using solutions of ca. 15 mg cm⁻³ in CDCl₃. δ^{13} C reported herein were referenced to tetramethylsilane (TMS). These compounds were purchased from Sigma-Aldrich and used without further purification. All ¹³C NMR spectra, acquisition, and processing parameters are available in the ESI† (Fig. S2–S4). The experimental δ^{13} C for CHF₃, CF₃⁻, and all cations were obtained from the literature, ^{51,53} while those for the remaining anions were studied theoretically.

Computational details

Geometry optimizations and vibrational frequencies for all compounds were calculated using the Gaussian 09 program⁵⁴ within the coupled-cluster singles and doubles model. The aug-cc-pVTZ basis set⁵⁵ was selected for all atoms, except iodine, for which the version with pseudopotential⁵⁶ was chosen. All structures reported in this article are true energy minima on the potential energy surface.

¹³C shielding tensors were calculated within the gaugeincluding atomic orbital (GIAO) framework through the NMR module of the Amsterdam Density Functional suite (ADF, version 2018). 57-60 The level of theory utilized for the decomposition analyses of σ^{13} C was chosen after a calibration study for neutral and cationic derivatives. The accuracy of the calculated δ^{13} C was evaluated by testing different functionals (KT2, OLYP, OPBE, PBE, PW91, B1PW91, B3LYP, OPBE0, and PBE0) and Slater-type orbital all-electron basis sets⁶¹ (TZ2P, TZ2P-J, ATZ2P, QZ3P-1D, QZ4P, and QZ4P-J), as well as the effect of implicit solvent and the inclusion of SO-specific self-consistent contributions from the DFT exchange-correlation response kernel (f_{XC}) .⁶² The solvent effects were incorporated by applying the conductor-like screening model (COSMO)⁶³ with parameters for chloroform. Relativistic corrections were made via the zeroth-order regular approximation (ZORA). 64-66 The level of theory with better agreement to the experimental δ^{13} C values, determined for neutral and cationic derivatives, was also applied to the study of anions. The δ^{13} C was calculated with CH₄ as a secondary reference:

$$\delta_i = \sigma_{\text{CH}_A} - \sigma_i + \delta_{\text{CH}_A} \tag{2}$$

where σ_i is the calculated shielding of the carbon nucleus of interest, and σ_{CH_4} and δ_{CH_4} are the calculated carbon shielding constant and the experimental chemical shift of methane, respectively. The δ_{CH_4} was obtained from the literature⁶⁷ and referenced to TMS. We used a secondary reference in the calculation to take advantage of the cancellation of errors, but all trends studied herein are not at all affected by the choice of reference.

The shielding mechanisms were identified through the splitting of σ^{13} C into σ^{dia} , σ^{para} , and σ^{SO} terms, as mentioned in the introduction section. Each term was rationalized following the decomposition analyses²⁵ of σ^{13} C into contributions from scalar-relativistic (SR) natural localized molecular orbitals (NLMO) and canonical molecular orbitals (CMO) generated by

the NBO 6.0 program.⁶⁸ The $\sigma^{\rm para}$ and $\sigma^{\rm SO}$ terms are not determined separately in the LMO analysis, so to analyze individual orbital contributions to $\sigma^{\rm SO}$ we subtracted the sums $(\sigma^{\rm para} + \sigma^{\rm SO})$ calculated at the SO-ZORA and SR-ZORA levels. Therefore, in this work, the $\sigma^{\rm para}$ refers to the paramagnetic shielding obtained from the SR-ZORA calculation, whereas the $\sigma^{\rm SO}$ is given as the difference between SO-ZORA and SR-ZORA calculations.

The spin-orbit effects on the σ^{13} C are variationally calculated in the ADF NMR module using a full set of scalar (spin-free) NLMOs to analyze it. In this analysis, both occupied and unoccupied NLMOs of the spin-free system are needed to describe the spin-orbit effect on the ground state electronic structure. ^{25,69} These effects are related to the mixture of orbitals with different symmetry, changes in orbital shapes, and the spin density induced by the external magnetic field. Therefore, the description of spin-density in our scalar NLMO analysis requires contributions from unoccupied or antibonding orbitals.

The effect of magnetic field orientation relative to the molecule was investigated by considering the principal components (σ_{11} , σ_{22} , and σ_{33}) of the σ^{13} C in its molecule-fixed principal axis system (PAS). Polar plots of σ^{13} C were prepared according to ref. 70 and 71.

Results and discussion

Calibration

The benchmark study of δ^{13} C shows that the level of theory B1PW91/QZ4P, including the implicit solvent and $f_{\rm XC}$, accurately reproduces the experimental values for neutral and cationic compounds (Fig. 2a). The root mean square deviation (RMSD) values of 6.56 ppm and 8.00 ppm for CHX₃ and CX₃⁺, respectively, in a range of almost 400 ppm are suitable for the study of molecules containing HAs. Similar deviations were obtained by Samultsev *et al.*⁴² for CHX₃ systems, even considering 4-component relativistic methods. The results obtained with other functionals and basis sets are collected and discussed in Section 3 of the ESI.†

Fig. 2a displays a linear NHD for the neutral series and a non-linear NHD for cations. The δ^{13} C of $\mathrm{CX_3}^+$ increases when going from $\mathrm{F^{35}}$ to Cl and then decreases to I. On the other hand, the anion series follows neither NHD nor the same trend as that observed for $\mathrm{PX_3}$, 52 but IHD (Fig. 2b). All combinations of DFT's variables (functionals, basis set, solvent, f_{XC}) tested in the present article exhibit the same behavior for the $\mathrm{CX_3}^-$ series. However, as shown in Fig. 2b, hybrid functionals show a more intense increase of $\delta^{13}\mathrm{C}$ for $\mathrm{CI_3}^-$ in comparison to GGA ones. The main difference between these calculations corresponds to the impact of f_{XC} on hybrid functionals. We expected that the inclusion of f_{XC} improves the SO contribution, and hence the accuracy of $\delta^{13}\mathrm{C}$ of anions, similar to that observed for the bromine and iodine derivatives of $\mathrm{CHX_3}$ and $\mathrm{CX_3}^+$ (see Section 3 of the ESI†). It is important to state that the trend for anions

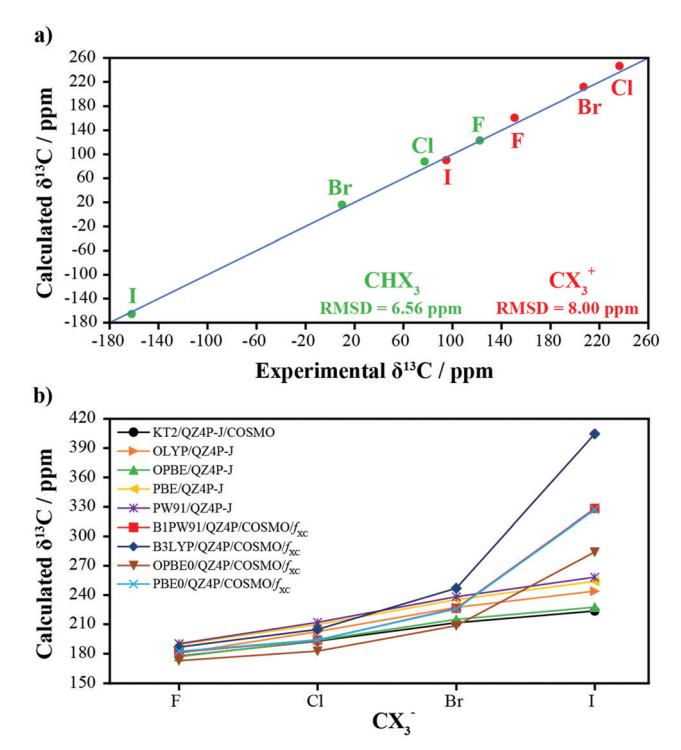


Fig. 2 (a) Correlation of the calculated (B1PW91/QZ4P/COSMO/ $f_{\rm XC}$) versus experimental δ^{13} C for the neutral and cationic derivatives of trihalomethane. (b) The δ^{13} C of trihalomethyl anions calculated with different levels of theory. Each line corresponds to the best level found for each functional in the calibration study of neutral and cationic derivatives. See all results in Section 3 of the ESI.†

analyzed herein is a prediction since only the experimental $\delta^{13}{\rm C}$ of ${\rm CF_3}^-$ is known.

Trends for the isotropic shielding tensor

In the following, we decide to focus our discussion more on σ trends than δ ones. Therefore, it is important that the reader keeps in mind the inverse relation between δ and σ to avoid any misunderstanding. Fig. 3 re-states the halogen dependence of the three studied systems in terms of σ : an increase of shielding tensor across the CHX $_3$ and CX $_3^+$ series, and a decrease for the CX $_3^-$ one. These results are displayed as a difference $(\Delta\sigma)$, relative to the fluorine derivative of each system, to allow easier visualization of trends. The corresponding values are provided in Tables S12 and S13 in the ESI.† Fluorinated compounds were studied previously by us; 40 however, the data displayed here were recalculated using the same level of theory for the whole halogen series.

A more detailed analysis of σ indicates that the NHD across the neutral series is four times more intense than that in cations. As expected, the $\sigma^{\rm SO}$ strongly increases in both CHX₃ and CX₃⁺ series with increasing Z_X ; however, the $\sigma^{\rm para}$ shows opposite behaviors. While the $\sigma^{\rm para}$ becomes less negative $(\Delta \sigma^{\rm para} > 0$, Fig. 3a) for the CHX₃ series, a pronounced increase in its magnitude $(\Delta \sigma^{\rm para} < 0$, Fig. 3b) is observed for CX₃⁺. This increase of $\sigma^{\rm para}$ explains the smaller and non-linear NHD in the cationic series, *i.e.*, the $\sigma^{\rm para}$ dominates the deshielding

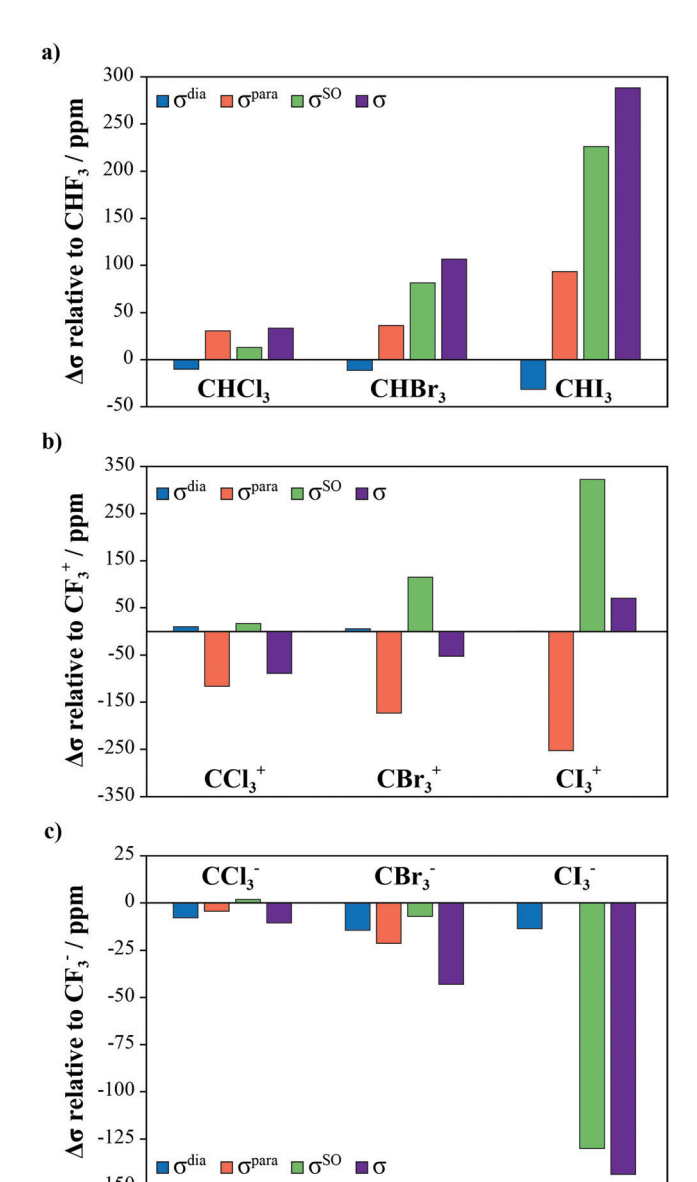


Fig. 3 Diamagnetic (σ^{dia}), paramagnetic (σ^{para}), and spin-orbit (σ^{SO}) contributions to the carbon shielding tensor (σ) for (a) CHX₃, (b) CX₃⁺, and (c) CX₃⁻. All values are relative to the respective fluorinated derivative and are shown in Table S12 (ESI†). Note the particular scale of each plot.

variation for Cl, but the $\sigma^{\rm SO}$ reduces this effect for Br and overcomes it for I. This paramagnetic effect prevents the NHD of cations from being larger than that observed for neutral compounds since the carbon of the former has a higher s-character increasing the spin–orbit contribution. On the other hand, both $\sigma^{\rm para}$ and $\sigma^{\rm SO}$ variations contribute to a larger and linear NHD for CHX₃.

Despite some changes, the $\sigma^{\rm dia}$ trend does not follow the NHD, and it is not decisive for the CHX₃ and almost invariant for CX₃⁺. Therefore, the remaining discussion about CHX₃ and CX₃⁺ series focuses on the $\sigma^{\rm para}$ and $\sigma^{\rm SO}$ components.

Regarding anions, the three contributions play a role in the IHD (Fig. 3c). The $\sigma^{\rm dia}$ decreases for heavier halogens, which is essential to understand the inverse trend in CCl₃⁻ and CBr₃⁻.

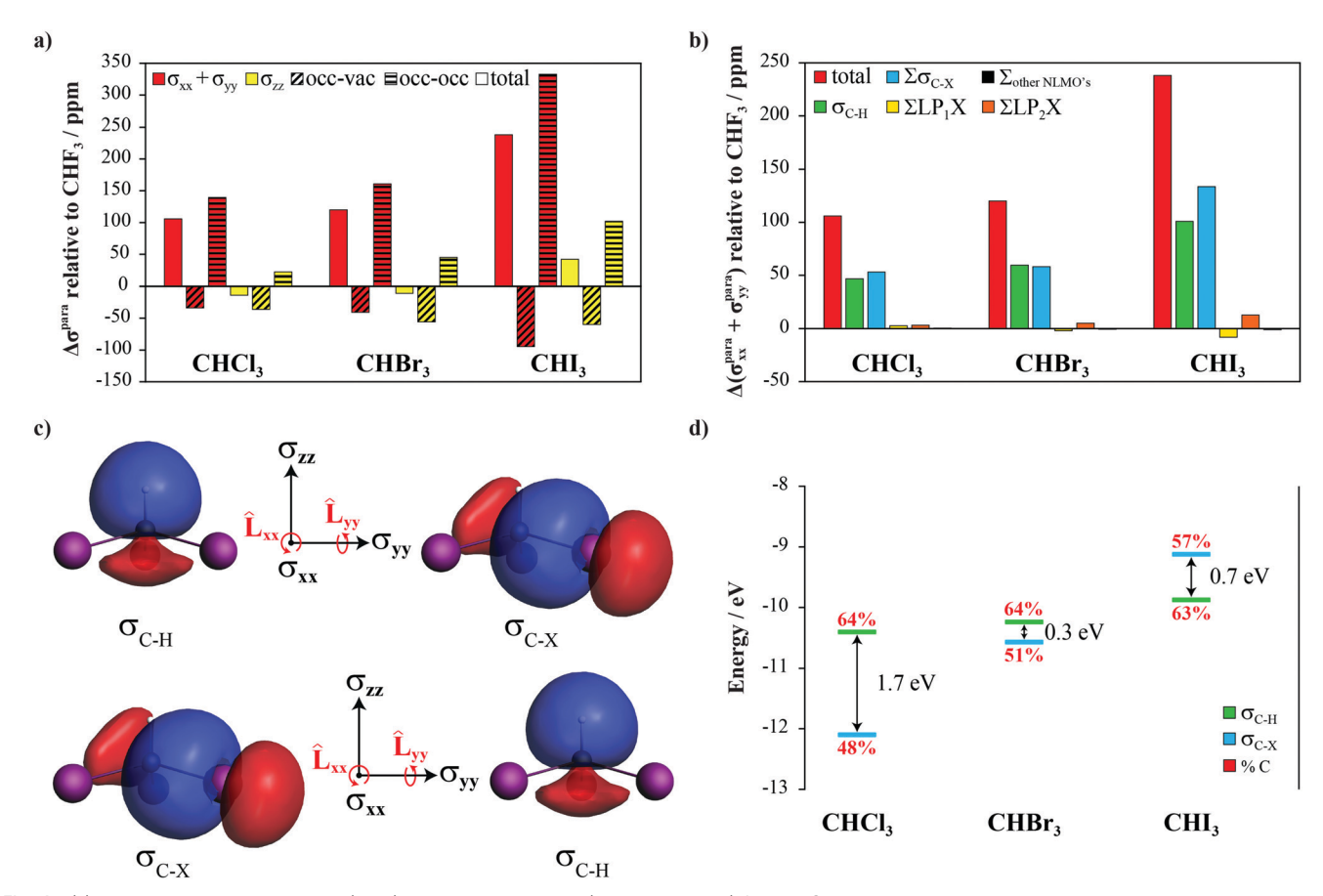


Fig. 4 (a) Paramagnetic contributions (total) along principal axes (σ_{xx} , σ_{yy} , and σ_{zz}) for the CHX₃ series. Each contribution is split into values that arise from couplings between occupied and vacant MOs (occ-vac), and between two occupied MOs (occ-occ). (b) NLMO contributions to the sum of σ_{xx} and σ_{yy} components of σ^{para} . (c) Isosurfaces (0.02 a.u.) and (d) energy levels of orbitals that couple upon the action of an external magnetic field.

There is no trend for σ^{para} across the series, which can indicate the competition between paramagnetic mechanisms. The σ^{para} becomes more negative for Br; however, it returns to the initial value for I. The pronounced decrease of σ for CI_3^- is described interestingly by negative spin-orbit contributions instead of scalar paramagnetic ones, as usually expected for IHD trends.³³ The σ^{SO} is positive and small for Cl when compared to the neutral and cationic ones, but becomes negative for Br and large in magnitude for I. This behavior could indicate the competition between positive and negative spin-orbit mechanisms across the halogen series.

These observations regarding the $\sigma^{\rm para}$ and $\sigma^{\rm SO}$ of the CX₃ series are the main findings of the article since negative SO contributions on carbon nuclei from heavy halogens are unexpected.

Orbital contributions to the σ^{para}

Having established which contributions are responsible for the three halogen dependences, we focus now on decomposing each mechanism into principal components and orbital contributions. All orbital contributions to the $\sigma^{\rm dia}$, $\sigma^{\rm para}$, and $\sigma^{\rm SO}$ components are, respectively, collected in Sections 5-7 of the ESI.† We named principal components according to their orientation relative to the molecular cartesian coordinates

 $(\sigma_{xx}, \sigma_{yy}, \text{ and } \sigma_{zz})$ to allow easier comparison between compounds. Furthermore, contributions from σ_{xx} and σ_{yy} axes are displayed in this work as a sum because they are equal due to the symmetry of the molecules. σ_{xx} and σ_{yy} axes lie in the plane of $\sigma_{\text{C-X}}$ bonds for CX_3^{+} and above them for CHX_3 and CX_3^{-}, while the σ_{zz} axis aligns with the σ_{C-H} bond in CHX₃, with the π_{C-X} in CX_3^+ , and with the LP C in CX_3^- .

We decomposed the σ^{para} in terms of molecular orbital (MO) and natural localized molecular orbital (NLMO) contributions. Analyses in terms of MO provide which pair of perpendicular orbitals generates paramagnetic shielding. However, these contributions are dispersed in several MOs, and each one is composed of a mixture of localized orbitals. Analyses in terms of NLMO concentrate contributions in a few orbitals, but we lose information about which pairs of orbitals are magnetically coupled. Therefore, we performed both analyses to get an intuitive picture of the main magnetic couplings.

A thorough investigation of MO contributions to the principal components reveals that σ_{xx} and σ_{yy} describe the downward trend in the magnitude of σ^{para} observed in CHX₃ (Fig. 4a). Changes in σ_{zz} are also present but less significant. Fig. 4a indicates that couplings between pairs of occupied MOs (occ-occ) are responsible for the changes in the σ^{para} . Contributions from these couplings have a positive sign (Table S30, ESI†) and exhibit an

increase across the series. Couplings involving occupied and vacant MOs (occ–vac) become more effective for heavier compounds; however, this negative increase is less pronounced. It is common to associate changes in $\sigma^{\rm para}$ with occ–vac couplings, but interestingly it is not the case of the neutral series.

In terms of NLMOs, magnetic couplings arise from the contributions of $\sigma_{\text{C-H}}$ and $\sigma_{\text{C-X}}$ orbitals (Fig. 4b). The action of the \hat{L}_i operator along the σ_{xx} and σ_{yy} axes generates magnetic couplings between occupied $\sigma_{\text{C-H}}$ and $\sigma_{\text{C-X}}$ orbitals, as shown in Fig. 4c. The shielding effect caused by these couplings increases for heavier halogens due to a decrease in the energy gap and a high polarization of $\sigma_{\text{C-X}}$ orbitals towards the carbon atom (Fig. 4d). The larger orbital coefficient on carbon for the CHI₃ molecule is the main reason for the less negative σ^{para} in the neutral series.

In contrast, the strong deshielding effect observed for σ^{para} in the cationic series is described by occ–vac couplings that perturbed the carbon nuclei in the σ_{xx} and σ_{yy} components (Fig. 5a). These occ–vac couplings contribute negatively to σ^{para} (Table S32, ESI†) and show a pronounced increase in its magnitude across the CX_3^+ series. The $\sigma_{\text{C-X}}$ orbitals are responsible for more than 80% of the trend, while the contributions of $\pi_{\text{C-X}}$, LP₁X, and LP₃X orbitals increase the magnitude of σ^{para} on a small scale (Fig. 5b). Occ–vac interactions involving $\sigma_{\text{C-X}}$ orbitals are intense in cations due to the presence of the

low-lying vacant π^*_{C-X} orbital perpendicular to the C–X bond with a high coefficient on the carbon atom (Fig. 5c). The paramagnetic effect generated by the coupling between σ_{C-X} and π^*_{C-X} increases across the series as a result of decreasing the energy gap between them (Fig. 5d) caused by the increase of the σ_{C-X} energy. Moreover, the coefficient of the σ_{C-X} orbital towards the carbon atom increases for heavier halogens, which generates magnetic couplings closer to the carbon nuclei.

Other couplings such as $\pi_{\text{C-X}} - \sigma^*_{\text{C-X}}$, $\text{LP}_1 X - \pi^*_{\text{C-X}}$, and $\text{LP}_3 X - \sigma^*_{\text{C-X}}$ are also observed when the \hat{L}_i operates in σ_{xx} and σ_{yy} axes. These couplings are weaker than the $\sigma_{\text{C-X}} - \pi^*_{\text{C-X}}$ ones because $\sigma^*_{\text{C-X}}$ is a worse acceptor than $\pi^*_{\text{C-X}}$ and $\text{LP}_1 X$ and $\text{LP}_3 X$ NLMOs have small coefficients on the carbon atom. However, the energy gap for these three magnetic couplings also decreases across the series (Table S37, ESI†), increasing the deshielding effect in CBr_3^+ and CI_3^+ .

To understand the σ^{para} in anions, it is important to consider that paramagnetic couplings are weakened in orbitals with a higher s-character since there is no effect of \hat{L}_i on s orbitals. The s-character of carbon orbitals in anions is concentrated to a large extent in the LP C, while the C–X bonds have mostly a p-character. Table S40 (ESI†) shows that the s-character varies in a range of 60–80% for LP C and 6–15% for $\sigma_{\text{C-X}}$ bonds.

The non-linear behavior of σ^{para} across the series arises from the changes in the three principal components, but the overall

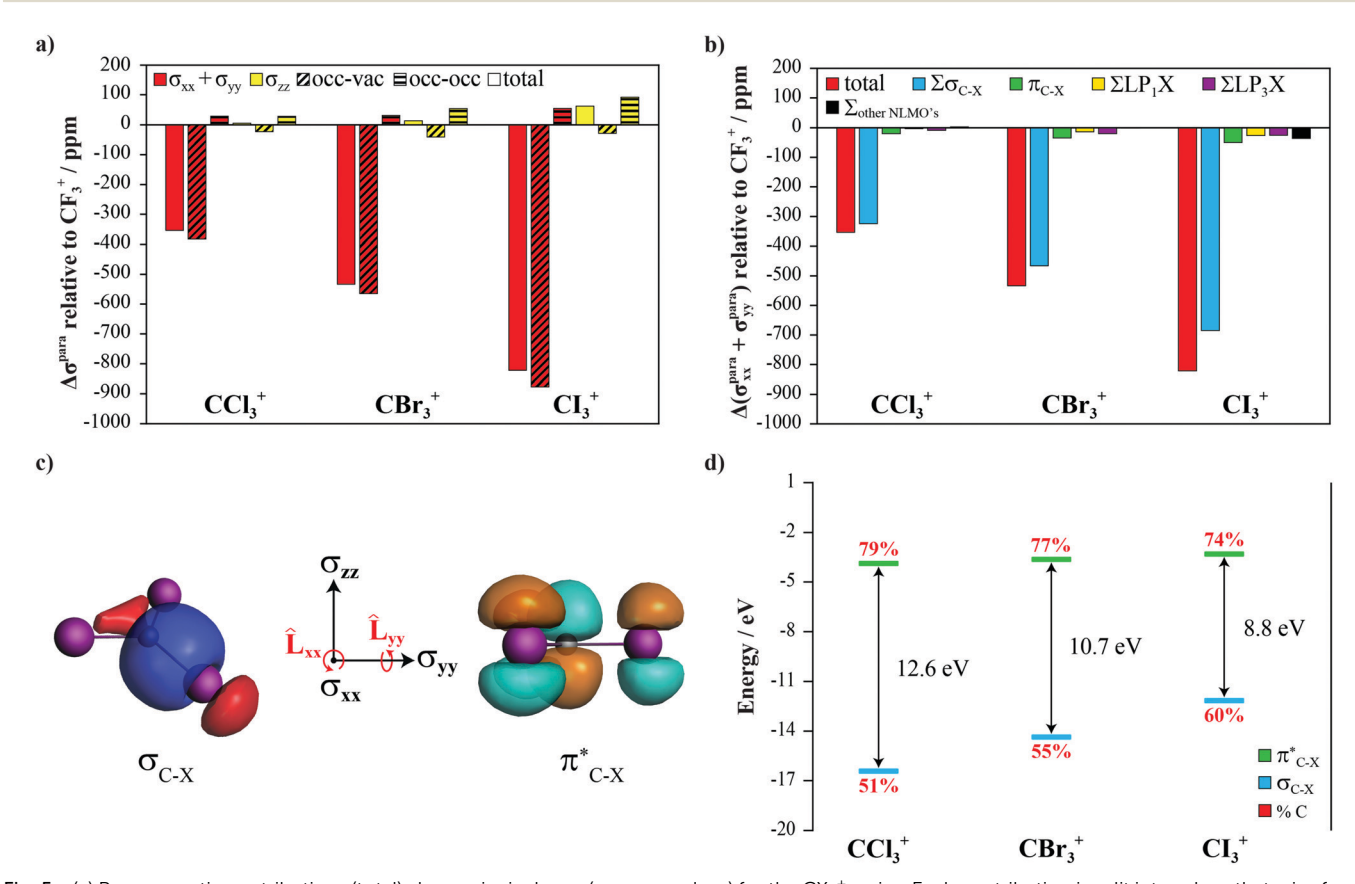


Fig. 5 (a) Paramagnetic contributions (total) along principal axes (σ_{xx} , σ_{yy} , and σ_{zz}) for the CX₃⁺ series. Each contribution is split into values that arise from couplings between occupied and vacant MOs (occ–vac), and between two occupied MOs (occ–occ). (b) NLMO contributions to the sum of σ_{xx} and σ_{yy} components of σ^{para} . (c) Isosurfaces (0.03 a.u.) and (d) energy levels of orbitals that couple upon the action of an external magnetic field.

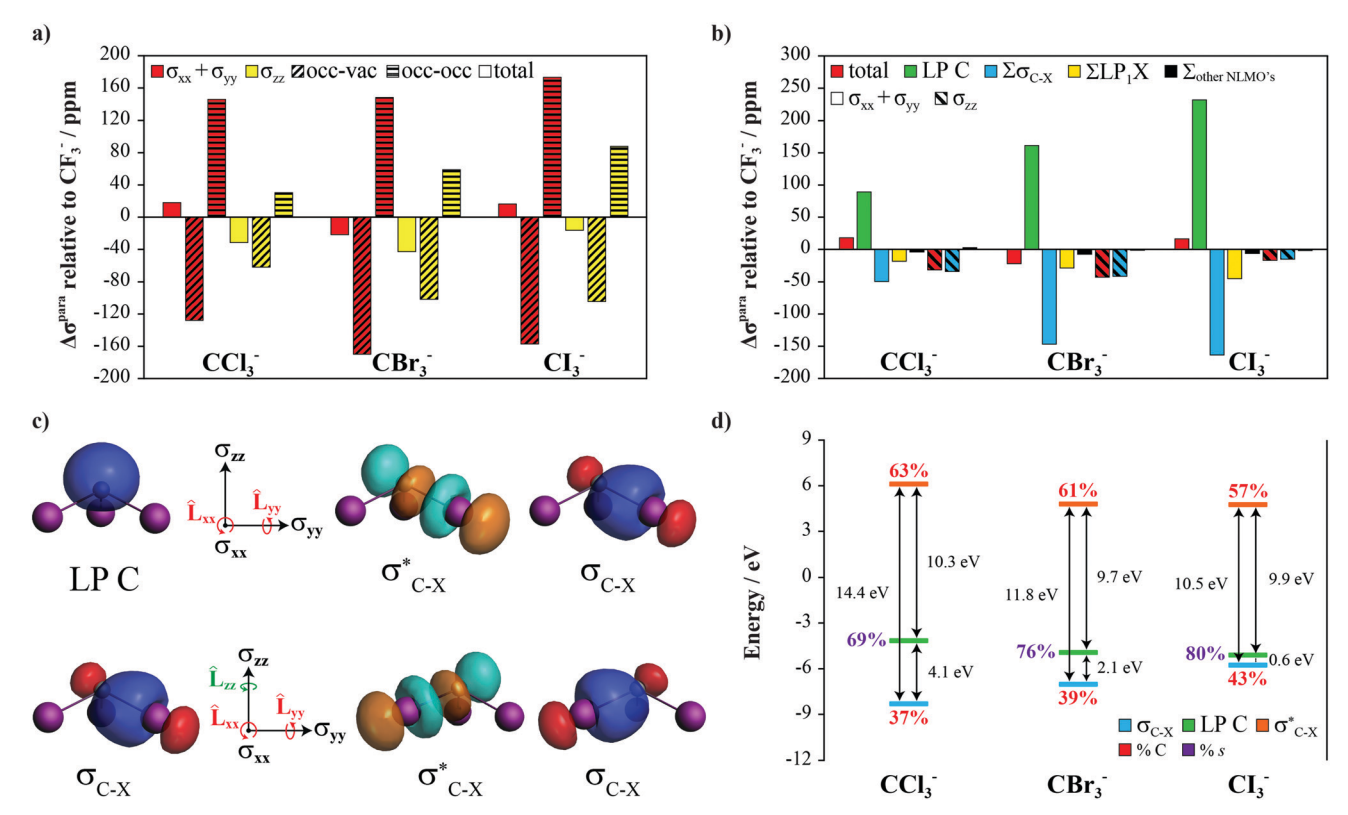


Fig. 6 (a) Paramagnetic contributions (total) along principal axes (σ_{xx} , σ_{yy} , and σ_{zz}) for the CX₃⁻ series. Each contribution is split into values that arise from couplings between occupied and vacant MOs (occ-vac), and between two occupied MOs (occ-occ). (b) NLMO contributions to the principal components of σ^{para} . (c) Isosurfaces (0.04 a.u.) and (d) energy levels of orbitals that couple upon the action of an external magnetic field.

trend is better reproduced by the σ_{zz} one (Fig. 6a). The values of σ^{para} are more negative in σ_{xx} and σ_{yy} components; however, the small variation in the CX₃⁻ series is a consequence of the cancellation between positive and negative trends observed for occ-occ and occ-vac couplings, respectively.

The magnitudes of occ-occ and occ-vac couplings in σ_{xx} and $\sigma_{\nu\nu}$ components rise significantly for CCl_3^- , but only a small variation is observed for heavier derivatives (Table S34, ESI†). These behaviors are described by the opposite trends of LP C, σ_{C-X} , and LP₁X orbital contributions (Fig. 6b). In our previous article, 40 we showed that the coupling between LP C and σ^*_{C-F} orbitals in $\mathrm{CF_3}^-$ is magnetically induced along σ_{xx} and σ_{yy} axes, generating a strong deshielding effect. The LP C - σ^*_{C-X} coupling (Fig. 6c) is also important for the $\sigma^{\rm para}$ of the other CX₃⁻ compounds, but its magnitude decreases. There are two reasons for the $\Delta\sigma^{\mathrm{para}} > 0$ of LP C contributions across the series: (1) the LP C – σ^*_{C-X} coupling is less efficient and (2) the LP C – σ_{C-X} coupling increases and has a positive sign. The first magnetic interaction decreases across the series because the s-character of the LP C orbital increases and the coefficient of $\sigma^*_{\text{C--X}}$ towards the carbon atom decreases, despite the reduction of the energy gap between coupled orbitals (Fig. 6d). The occ-occ coupling between LP C and σ_{C-X} orbitals increases across the series due to the decrease in the energy gap and higher polarization to the carbon atom of σ_{C-X} orbitals in heavier compounds; however, this increase is minimized by the high s-character of LP C in CBr_3^- and CI_3^- .

The σ_{C-X} and LP₁X contributions show $\Delta \sigma^{para} < 0$ in σ_{xx} and σ_{yy} components which practically cancels the effect of LP C. For these orbitals, the effect of occ-vac couplings overcomes that of the occ-occ ones, leading to a negative change in the σ^{para} . Fig. 6c displays only the magnetic interaction between the σ_{C-X} and σ^*_{C-X} of different bonds, but similar coupling occurs with LP₁X. The lowering of the energy gap (Fig. 6d) and high p-character of σ_{C-X} bonds (Table S40, ESI†) favor the occ-vac coupling despite the fact that the occ-occ σ_{C-X} - LP C reduces the increase from CBr₃⁻ to CI₃⁻.

The interpretation of the σ_{zz} component is less complex than that of σ_{xx} and σ_{yy} because only the σ_{C-X} orbitals are responsible for changes. As the LP C is pointing along the σ_{zz} , its contribution is almost zero. The $\sigma_{\text{C-X}}$ orbitals can couple to the σ^*_{C-X} and σ_{C-X} of different bonds upon the action of \hat{L}_i along σ_{zz} . Both induced interactions increase across the series, but the magnitude of occ-vac coupling overcomes that of the occ-occ one. The $\mathrm{CBr_3}^-$ displays larger σ^para than other anions because occ-vac couplings are predominant in the three principal components.

Orbital contributions to the σ^{SO}

We analyze the σ^{SO} using molecular spinor pairs (MSPs) and also its decomposition in NLMOs. Analyses in terms of MSP allow identifying couplings between occupied and vacant MSPs while accounting for SO effects and provide differences from scalar analogous MO-MO couplings.

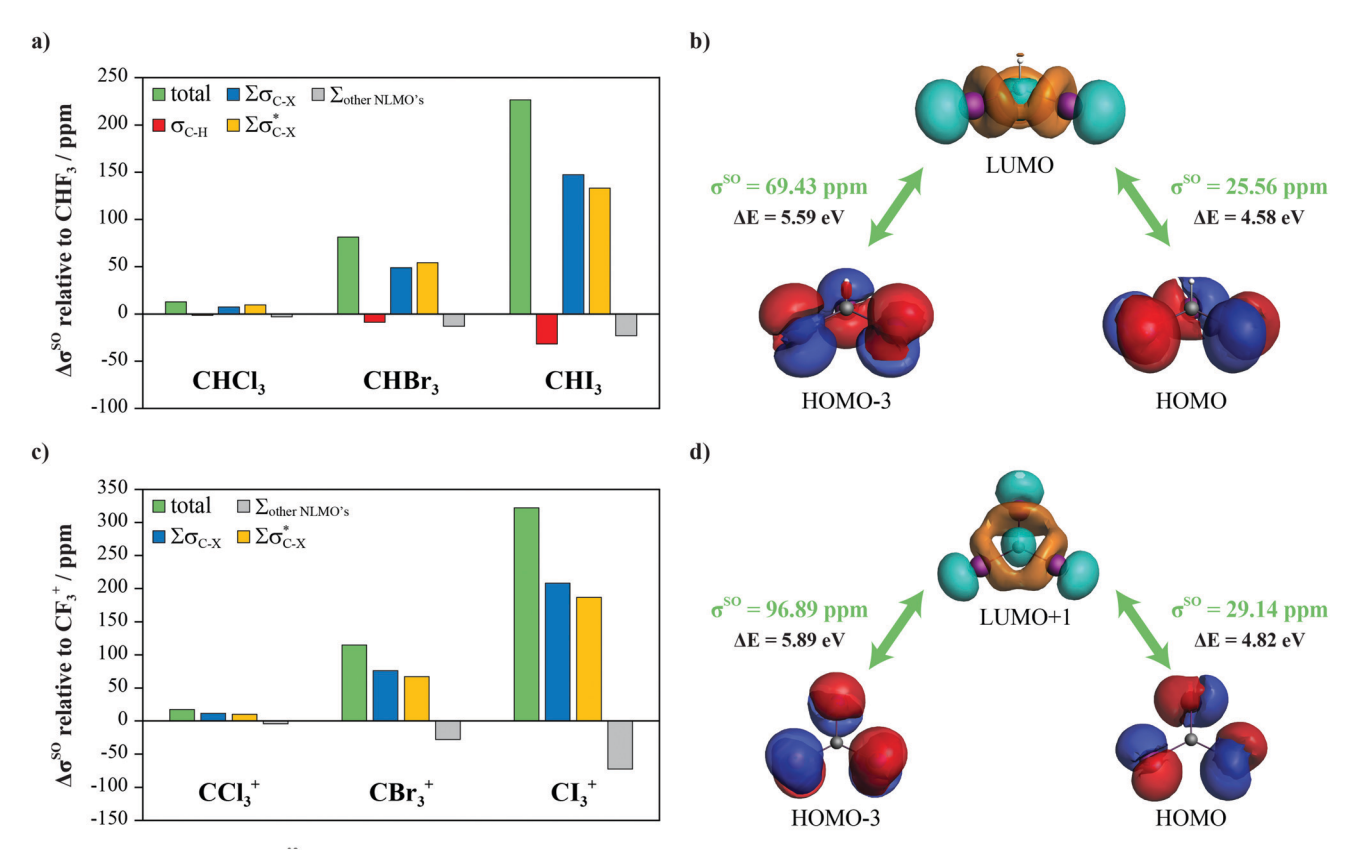


Fig. 7 NLMO contributions to σ^{SO} for (a) neutral and (c) cationic series. Isosurfaces (0.03 a.u.) of MSPs that couple and transmit the SO-HALA effect from the iodine atom to the carbon nucleus in (b) CHI₃ and (d) CI₃⁺ molecules.

As expected, the magnitude of σ^{SO} increases with the increase of halogen nuclear charge (Z) in all series. This effect is observed in the three principal orientations of σ , but it is much more pronounced in the σ_{zz} component (see Section 6 of the ESI†). The SO coupling induces mixing of orbitals of different symmetry for the three series, but the carbon nucleus undergoes a shielding response in neutral and cationic series, whereas a deshielding response prevails in anions, especially in CI_3^- .

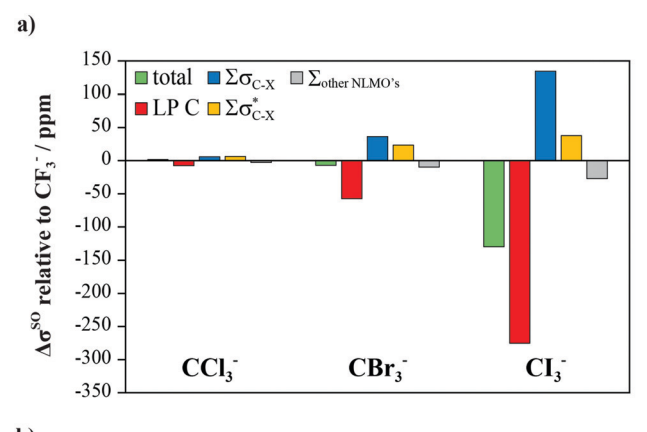
The σ^{SO} of neutral and cationic series are described by contributions from σ_{C-X} and σ^*_{C-X} orbitals as shown in Fig. 7a and c, respectively. The valence σ_{C-X} orbitals contribute to σ^{SO} due to the s-character of the C–X bond being sufficient to allow efficient transmission of the SO/FC mechanism. As the s-character of σ_{C-X} orbitals is larger in CX_3^+ than that in CHX₃, the SO effect is more intensely experienced by the carbon nucleus of cations. Contributions from σ^*_{C-X} NLMOs arise because unoccupied orbitals of the spin-free system are required to describe the spin–orbit effect on the ground state electronic structure, *i.e.*, these values could be interpreted as a requirement of the NLMO analysis to describe the spin density at the HA that propagates to carbon through the SO/FC mechanism.

The two main couplings responsible for the σ^{SO} values of CHI₃ and CI₃⁺ involve the HOMO-3 and HOMO MSPs with the LUMO and LUMO+1 MSPs of neutral and cationic series,

respectively (Fig. 7b and d). HOMO-3 and HOMO MSPs contain a mixture of halogen nonbonding MOs that propagate the SO effect to the corresponding vacant MSP having significant scharacter on carbon. The presence of filled nonbonding MSPs in the valence shell of the halogen usually causes shielding contribution to the SO/FC mechanism. ²⁹ Other couplings involving occupied MSPs with a high percentage of the σ_{C-X} orbital also couple with the LUMO/LUMO+1 MSP participating in the SO/FC pathways (Table S36, ESI†).

The σ^{SO} trend calculated for the anion series is a consequence of two spin–orbit transmission mechanisms that subtract each other. Positive or shielding contributions are obtained by σ_{C-X} and σ^*_{C-X} orbitals (Fig. 8a) and correspond to a similar mechanism to that determined in neutral and cationic derivatives. However, the large p-character of the C–X bond in anions leads to an inefficient SO/FC pathway and, consequently, to a small magnitude of this positive contribution. Analyses of MSPs indicate that the shielding effect is transmitted through a coupling between HOMO–3 and LUMO MSPs (Fig. 8b).

The SO deshielding contribution arises from the LP C orbital. The large s-character of LP C allows efficient transmission of the SO/FC mechanism that cancels the positive contribution in CBr₃⁻ and intensely overcomes it in CI₃⁻. The coupling between the HOMO, formed by carbon and halogen nonbonding orbitals, and the LUMO has a negative contribution and a small energy gap.



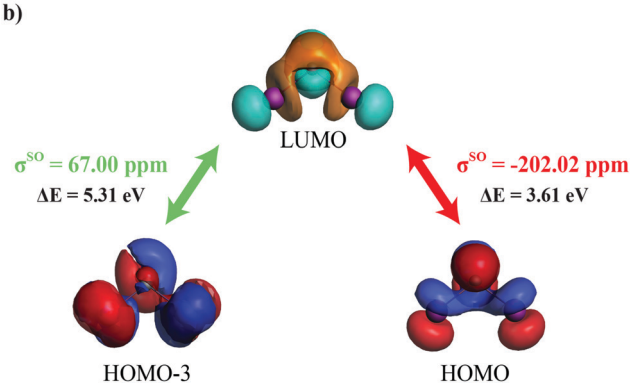


Fig. 8 (a) NLMO contributions to σ^{SO} for the anion series. (b) Isosurfaces (0.03 a.u.) of MSPs that couple and transmit the SO-HALA effect from the iodine atom to the carbon nucleus in Cl₃⁻.

This result indicates that the high electronic density on carbon affects the sign of the SO/FC mechanism in a significant magnitude. The HOMO-LUMO coupling is the main reason for IHD in the anion series.

Orbital contributions to the σ^{dia} of anions

As mentioned before, the σ^{dia} component is important to understand the IHD in CCl_3^- and CBr_3^- . Changes in σ^{dia} across the series are not large, but variations of σ^{para} and σ^{SO} are even smaller for CCl_3^- and comparable for CBr_3^- . The carbon core orbital is the main contribution of σ^{dia} , but its value does not vary in the series (Table S14, ESI†). According to Table 1, the LP C is responsible for the decrease of σ^{dia} in CCl_3^- , while the σ_{C-X}

Table 1 NLMO contributions ab to the $\sigma^{\rm dia}$ component of $\sigma^{\rm 13}{\rm C}$ for the CX₃⁻ series^c

| NLMO | CCl ₃ ⁻ | $\mathrm{CBr_3}^-$ | ${ m CI_3}^-$ |
|--------------------------|-------------------------------|--------------------|---------------|
| $\Sigma \sigma_{C-X}$ | 1.42 | -6.04 | -5.41 |
| LP C | -6.59 | -4.43 | -2.91 |
| ΣLP_1X | -1.10 | -1.92 | -2.06 |
| ΣLP_2X | -0.48 | -0.49 | -1.12 |
| ΣLP_3X | -1.05 | -1.35 | -2.43 |
| $\Sigma_{ m otherNLMOs}$ | -0.09 | -0.18 | 0.25 |
| $\Sigma_{ m all\ NLMOs}$ | -7.89 | -14.41 | -13.68 |

^a In ppm. ^b All values are relative to the respective fluorinated derivative and are shown in Table S14 (ESI). c X = Cl, Br, or I.

orbitals explain the trend for CBr₃⁻ and CI₃⁻. Small effects are also observed for the three halogen LPs.

The LP C orbital is more delocalized to the molecule in the CCl₃ (Table S38, ESI†) than in the other anions. This small occupancy on the carbon reduces the shielding effect of the LP C. For bromine and iodine derivatives, the LP C contribution is smaller than that in the fluorine one; however, this effect is less significant in comparison to CCl₂ due to the higher s-character of LP C in heavier compounds. In a complementary way, the increase of the p-character of σ_{C-X} orbitals across the series decreases the shielding effect in CBr₃⁻ and CI₃⁻. The increase of the σ_{C-X} orbital contribution for chlorine can be interpreted based on the decrease of electronegativity.

Anisotropic shielding tensor

Trends of $\sigma^{\rm dia}$, $\sigma^{\rm para}$, and $\sigma^{\rm SO}$ for each principal component when combined explain the changes in shielding surfaces observed across the halogen series (Fig. 9). In the CHX3 case, the shielding surfaces around carbon nuclei increase in all directions but more intensely in σ_{zz} as a consequence of the reduction of σ^{para} in σ_{xx} and σ_{yy} , and a remarkable increase of σ^{SO} in σ_{zz} . The opposite effect of σ^{para} and σ^{SO} in the CX₃⁺ series is evident when analyzing the graphical representation of shielding tensor (Fig. 9b). A deshielding surface in the xy plane, as we observed for CF₃⁺, ⁴⁰ becomes large across the series due to the increase of the magnitude of σ^{para} (more negative values) in σ_{xx} and σ_{yy} . In contrast, the σ^{SO} greatly increases the nuclear shielding along σ_{zz} , overcoming the values of other components in CI₃⁺. The values of all principal components decrease in the anion series, resulting in surfaces completely deshielding for CBr₃⁻ and CI₃⁻ compounds (Fig. 9c). This effect is more significant in σ_{zz} , mainly due to great negative σ^{SO} contributions to that orientation. The decrease of σ^{dia} across the series also contributes to the overall deshielding surface, especially from Cl to Br; however, this effect is very isotropic (Table S13, ESI†).

Conclusions

The δ^{13} C is commonly interpreted in organic chemistry and NMR textbooks through its direct association with electronic density and electronegativity concepts, mainly for charged molecules. However, this work shows that the σ is not related to the electronic density in a simple way since the carbon nucleus is more deshielding in CX_3^- than that in CX_3^+ when X is Br or I.

The information obtained from the orientation of σ combined with the knowledge of the orbital contributions allowed us to determine the origin of the unexpected IHD observed for the CX₃ series. Instead of scalar paramagnetic effects, the negative spin-orbit contribution from the carbon nonbonding orbital generates a deshielding effect on the carbon nucleus in heavier molecules. In contrast, positive spin-orbit contributions lead to an NHD for CHX₃ and CX₃⁺ series. Although the halogen dependence is already known for neutral and cationic series, we figure out the main magnetic couplings encoded in the tensor orientation of σ^{para} for both series. Couplings between pairs of occupied orbitals change more significantly

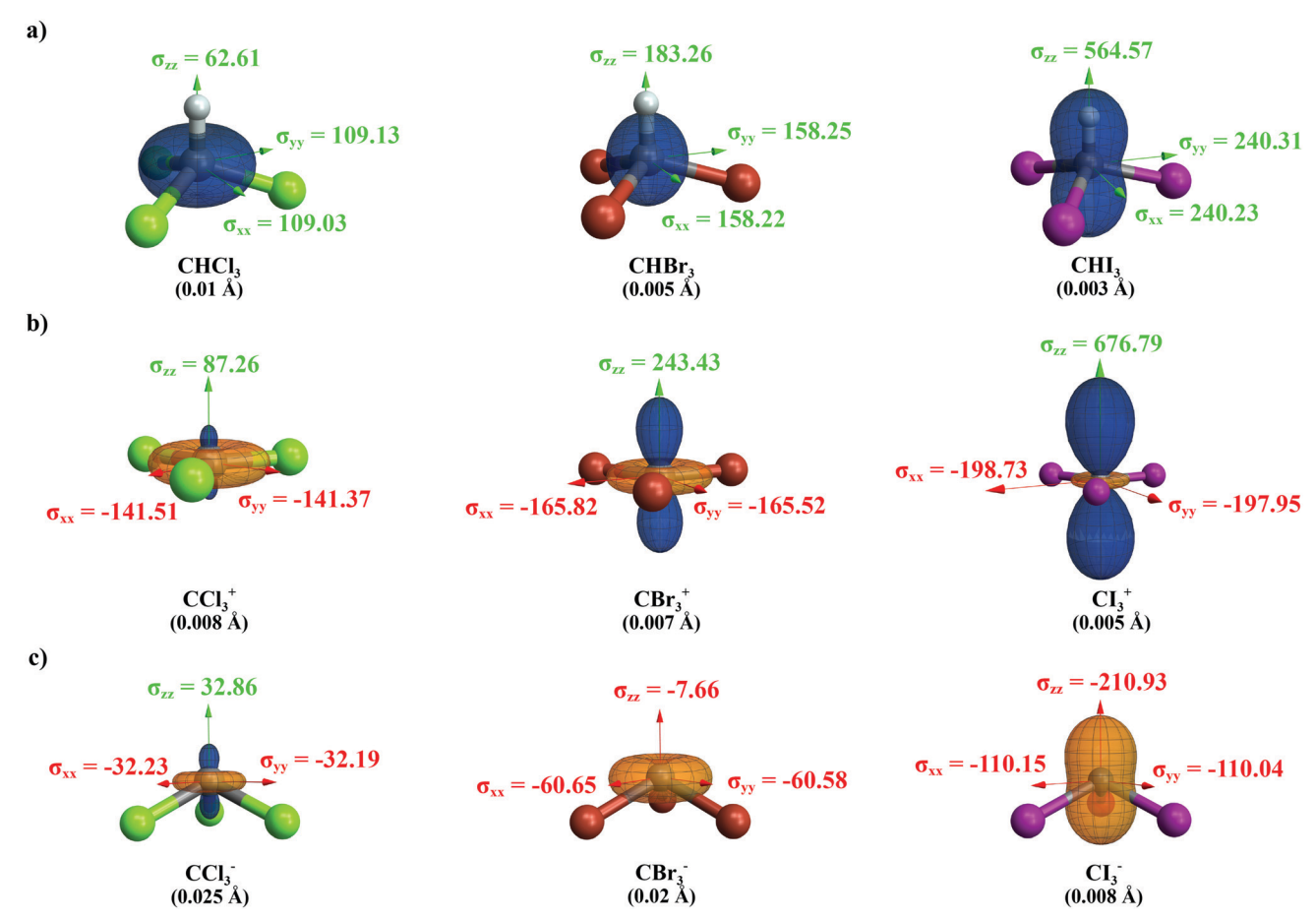


Fig. 9 Graphical representations of σ^{13} C for (a) CHX₃, (b) CX₃⁺, and (c) CX₃⁻ series. Green arrows and blue surfaces indicate nuclear shielding (positive values), while deshielding (negative values) is represented by red arrows and orange surfaces. Each surface is extended using a particular scaling factor listed in parentheses.

for the neutral series, while the coupling between occupied σ_{C-X} and unoccupied π^*_{C-X} explains the increase of the σ^{para} magnitude in the cationic series.

In summary, this work provides a guideline to interpret δ^{13} C in charged molecules. Instead of using the direct association with electronic density, we suggest the following: (1) cations show large δ^{13} C due to the presence of low-lying vacant orbitals that allow paramagnetic couplings with perpendicular occupied orbitals. Interactions involving these coupled orbitals can significantly affect their energy, and hence the δ^{13} C. (2) Anions have the LP C orbital of high energy that can generate a deshielding paramagnetic effect if good electron acceptor substituents are present. For molecules containing heavy atoms, anions can show large δ^{13} C due to the negative spin–orbit mechanism. (3) Neutral and saturated molecules tend to be more shielded than cations and anions due to small paramagnetic interactions generated by the occupied orbital with low energy and the vacant orbital with high energy.

Author contributions

R. V. V. performed the calculations and NMR measurements. All authors contributed to the analysis and discussions of the results and the preparation of the manuscript.

Conflicts of interest

There are no conflicts to declare.

Acknowledgements

We acknowledge the financial support from the São Paulo Research Foundation (grant #2015/08541-6 and #2020/10246-0, FAPESP) and scholarship to R. V. V. (grant #2017/20890-1, FAPESP). We are grateful for a fellowship from the National Council for Scientific and Technological Development (CNPq) to C. F. T. We thank Prof. Dr Lucas C. Ducati for providing access to the ADF2018 package. We also thank the National Laboratory for Scientific Computing (LNCC/MCTI, Brazil) for providing HPC resources of the SDumont supercomputer, which have contributed to the research results reported within this paper.

Notes and references

- 1 L. B. Krivdin, Magn. Reson. Chem., 2020, 58, 5-14.
- 2 L. B. Krivdin, Magn. Reson. Chem., 2020, 58, 15-30.

- 3 D. J. Milanowski, N. Oku, L. K. Cartner, H. R. Bokesch, R. T. Williamson, J. Saurí, Y. Liu, K. A. Blinov, Y. Ding, X.-C. Li, D. Ferreira, L. A. Walker, S. Khan, M. T. Davies-Coleman, J. A. Kelley, J. B. McMahon, G. E. Martin and K. R. Gustafson, Chem. Sci., 2018, 9, 307-314.
- 4 D. C. Burns and W. F. Reynolds, Magn. Reson. Chem., 2019, DOI: 10.1002/mrc.4933.
- 5 A. Navarro-Vázquez, R. R. Gil and K. Blinov, J. Nat. Prod., 2018, 81, 203-210.
- 6 M. R. M. Koos, A. Navarro-Vázquez, C. Anklin and R. R. Gil, Angew. Chem., Int. Ed., 2020, 59, 3938-3941 (Angew. Chem., 2020, 132, 3966-3969).
- 7 J. H. Simpson, Organic Structure Determination Using 2-D NMR Spectroscopy, Elsevier, Burlington, 2008.
- 8 K. C. Mullane, P. Hrobárik, T. Cheisson, B. C. Manor, P. J. Carroll and E. J. Schelter, Inorg. Chem., 2019, 58, 4152-4163.
- 9 J. Novotný, J. Vícha, P. L. Bora, M. Repisky, M. Straka, S. Komorovsky and R. Marek, J. Chem. Theory Comput., 2017, 13, 3586-3601.
- 10 M. M. Popa, I. C. Man, C. Draghici, S. Shova, M. R. Caira, F. Dumitrascu and D. Dumitrescu, CrystEngComm, 2019, 21, 7085-7093.
- 11 S. T. Holmes, O. G. Engl, M. N. Srnec, J. D. Madura, R. Quiñones, J. K. Harper, R. W. Schurko R. J. Iuliucci, J. Phys. Chem. A, 2020, 124, 3109-3119.
- 12 K. Sutter, G. A. Aucar and J. Autschbach, Chem. Eur. J., 2015, 21, 18138-18155.
- 13 J. Vícha, P. Švec, Z. Růžičková, M. A. Samsonov, K. Bártová, A. Růžička, M. Straka and M. Dračínský, Chem. - Eur. J., 2020, 26, 8698-8702.
- 14 A. C. Castro, M. Swart and C. Fonseca Guerra, Phys. Chem. Chem. Phys., 2017, 19, 13496-13502.
- 15 C. P. Gordon, S. Shirase, K. Yamamoto, R. A. Andersen, O. Eisenstein and C. Copéret, Proc. Natl. Acad. Sci. U. S. A., 2018, 115, E5867-E5876.
- 16 C. P. Gordon, D. B. Culver, M. P. Conley, O. Eisenstein, R. A. Andersen and C. Copéret, J. Am. Chem. Soc., 2019, 141, 648-656.
- 17 C. P. Gordon, K. Yamamoto, K. Searles, S. Shirase, R. A. Andersen, O. Eisenstein and C. Copéret, Chem. Sci., 2018, 9, 1912-1918.
- 18 C. P. Gordon, R. A. Andersen and C. Copéret, Helv. Chim. Acta, 2019, 102, e1900151.
- 19 M. H. Levitt, Spin dynamics: Basics of nuclear magnetic resonance, John Wiley & Sons, Chichester, 2nd edn, 2008.
- 20 L. J. Mueller, Concepts Magn. Reson., Part A, 2011, 38,
- 21 C. P. Gordon, C. Raynaud, R. A. Andersen, C. Copéret and O. Eisenstein, Acc. Chem. Res., 2019, 52, 2278-2289.
- 22 R. V. Viesser, L. C. Ducati, C. F. Tormena and J. Autschbach, Chem. Sci., 2017, 8, 6570-6576.
- 23 R. V. Viesser, L. C. Ducati, C. F. Tormena and J. Autschbach, Phys. Chem. Chem. Phys., 2018, 20, 11247-11259.
- 24 C. M. Widdifield and R. W. Schurko, Concepts Magn. Reson., Part A, 2009, 34A, 91-123.

25 J. Autschbach, J. Chem. Phys., 2008, 128, 164112.

- 26 J. Toušek, M. Straka, V. Sklenář and R. Marek, J. Phys. Chem. A, 2013, 117, 661-669.
- 27 C. B. Santiago, J.-Y. Guo and M. S. Sigman, Chem. Sci., 2018, 9, 2398-2412.
- 28 E. Pietrasiak, C. P. Gordon, C. Copéret and A. Togni, Phys. Chem. Chem. Phys., 2020, 22, 2319-2326.
- 29 J. Vícha, J. Novotný, S. Komorovsky, M. Straka, M. Kaupp and R. Marek, Chem. Rev., 2020, 120, 7065-7103.
- 30 J. Vícha, M. Straka, M. L. Munzarová and R. Marek, J. Chem. Theory Comput., 2014, 10, 1489-1499.
- 31 J. Autschbach and S. Zheng, Annu. Rep. NMR Spectrosc., 2009, 67, 1-95.
- 32 M. Kaupp, O. L. Malkina, V. G. Malkin and P. Pyykkö, Chem. - Eur. I., 1998, 4, 118-126.
- 33 M. Kaupp, in Relativistic Electronic Structure Theory Part 2. Applications, ed. P. Schwerdtfeger, Elsevier, 2004, vol. 14, pp. 552-597.
- 34 J. Vícha, S. Komorovsky, M. Repisky, R. Marek and M. Straka, J. Chem. Theory Comput., 2018, 14, 3025-3039.
- 35 S. Moncho and J. Autschbach, Magn. Reson. Chem., 2010, 48, S76-S85
- 36 M. Bühl, M. Kaupp, O. L. Malkina and V. G. Malkin, J. Comput. Chem., 1999, 20, 91-105.
- 37 Y. Y. Rusakov, I. L. Rusakova and L. B. Krivdin, Int. J. Quantum Chem., 2016, 116, 1404-1412.
- 38 J. B. Grutzner, J. M. Lawlor and L. M. Jackman, J. Am. Chem. Soc., 1972, 2328, 2306-2315.
- 39 K. B. Wiberg, J. D. Hammer, T. A. Keith and K. Zilm, Tetrahedron Lett., 1997, 38, 323-326.
- 40 R. V. Viesser and C. F. Tormena, Magn. Reson. Chem., 2020, **58**, 540-547.
- 41 S. Berger, U. Fleischer, C. Geletneky and J. C. W. Lohrenz, Chem. Ber., 1995, 128, 1183-1186.
- 42 D. O. Samultsev, Y. Y. Rusakov and L. B. Krivdin, Magn. Reson. Chem., 2016, 54, 787-792.
- 43 R. V. Viesser, L. C. Ducati, J. Autschbach and C. F. Tormena, Phys. Chem. Chem. Phys., 2015, 17, 19315-19324.
- 44 A. M. Kantola, P. Lantto, J. Vaara and J. Jokisaari, Phys. Chem. Chem. Phys., 2010, 12, 2679-2692.
- 45 M. Kaupp, O. L. Malkin and V. G. Malkin, Chem. Phys. Lett., 1997, 265, 55-59.
- 46 H. P. A. Mercier, M. D. Moran, G. J. Schrobilgen, C. Steinberg and R. J. Suontamo, J. Am. Chem. Soc., 2004, 126, 5533-5548.
- 47 I. Krossing, A. Bihlmeier, I. Raabe and N. Trapp, Angew. Chem., Int. Ed., 2003, 42, 1531-1534.
- 48 O. L. Malkina, B. Schimmelpfennig, M. Kaupp, B. A. Hess, P. Chandra, U. Wahlgren and V. G. Malkin, Chem. Phys. Lett., 1998, 296, 93-104.
- 49 W. M. Litchman and D. M. Grant, J. Am. Chem. Soc., 1968, 90, 1400-1407.
- 50 G. A. Olah, L. Heiliger and G. K. S. Prakash, J. Am. Chem. Soc., 1989, 111, 8020-8021.
- 51 G. A. Olah, G. Rasul, L. Heiliger and G. K. S. Prakash, J. Am. Chem. Soc., 1996, 118, 3580-3583.

- 52 T. A. Engesser, P. Hrobárik, N. Trapp, P. Eiden, H. Scherer, M. Kaupp and I. Krossing, *ChemPlusChem*, 2012, 77, 643–651.
- 53 G. K. S. Prakash, F. Wang, Z. Zhang, R. Haiges, M. Rahm, K. O. Christe, T. Mathew and G. A. Olah, *Angew. Chem., Int. Ed.*, 2014, 53, 11575–11578.
- 54 M. J. Frisch, G. W. Trucks, H. B. Schlegel, G. E. Scuseria, M. A. Robb, J. R. Cheeseman, G. Scalmani, V. Barone, B. Mennucci, G. A. Petersson, H. Nakatsuji, M. Caricato, X. Li, H. P. Hratchian, A. F. Izmaylov, J. Bloino, G. Zheng, J. L. Sonnenberg, M. Hada, M. Ehara, K. Toyota, R. Fukuda, J. Hasegawa, M. Ishida, T. Nakajima, Y. Honda, O. Kitao, H. Nakai, T. Vreven, J. A. Montgomery Jr, J. E. Peralta, F. Ogliaro, M. Bearpark, J. J. Heyd, E. Brothers, K. N. Kudin, V. N. Staroverov, R. Kobayashi, J. Normand, K. Raghayachari, A. Rendell, J. C. Burant, S. S. Iyengar, J. Tomasi, M. Cossi, N. Rega, J. M. Millam, M. Klene, J. E. Knox, J. B. Cross, V. Bakken, C. Adamo, J. Jaramillo, R. Gomperts, R. E. Stratmann, O. Yazyev, A. J. Austin, R. Cammi, C. Pomelli, J. W. Ochterski, R. L. Martin, K. Morokuma, V. G. Zakrzewski, G. A. Voth, P. Salvador, J. J. Dannenberg, S. Dapprich, A. D. Daniels, Ö. Farkas, J. B. Foresman, J. V. Ortiz, J. Cioslowski and D. J. Fox, Gaussian 09 (Revision D.01), Gaussian Inc., Wallingford CT, 2013.
- 55 T. H. Dunning Jr, J. Chem. Phys., 1989, 90, 1007-1023.
- 56 K. A. Peterson, J. Chem. Phys., 2003, 119, 11099-11112.
- 57 G. te Velde, F. M. Bickelhaupt, E. J. Baerends, C. Fonseca Guerra, S. J. A. van Gisbergen, J. G. Snijders and T. Ziegler, *J. Comput. Chem.*, 2001, 22, 931–967.

- 58 C. Fonseca Guerra, J. G. Snijders, G. te Velde and E. J. Baerends, *Theor. Chem. Acc.*, 1998, **99**, 391–403.
- 59 G. Schreckenbach and T. Ziegler, J. Phys. Chem., 1995, 99, 606–611.
- 60 *ADF2018*, SCM, Theoretical Chemistry, Vrije Universiteit, Amsterdam, The Netherlands, http://www.scm.com.
- 61 E. van Lenthe and E. J. Baerends, *J. Comput. Chem.*, 2003, 24, 1142–1156.
- 62 J. Autschbach, Mol. Phys., 2013, 111, 2544-2554.
- 63 C. C. Pye and T. Ziegler, *Theor. Chem. Acc.*, 1999, **101**, 396–408.
- 64 E. van Lenthe, E. J. Baerends and J. G. Snijders, *J. Chem. Phys.*, 1993, **99**, 4597–4610.
- 65 E. van Lenthe, E. J. Baerends and J. G. Snijders, *J. Chem. Phys.*, 1994, **101**, 9783–9792.
- 66 E. van Lenthe, J. G. Snijders and E. J. Baerends, *J. Chem. Phys.*, 1996, **105**, 6505–6516.
- 67 A. Antušek, K. Jackowski, M. Jaszuński, W. Makulski and M. Wilczek, *Chem. Phys. Lett.*, 2005, **411**, 111–116.
- 68 E. D. Glendening, J. K. Badenhoop, A. E. Reed, J. E. Carpenter, J. A. Bohmann, C. M. Morales, C. R. Landis and F. Weinhold, NBO 6.0, Theoretical Chemistry Institute, University of Wisconsin, Madison, 2013.
- 69 J. Autschbach and S. Zheng, Magn. Reson. Chem., 2008, 46, S45–S55.
- 70 E. Zurek, C. J. Pickard and J. Autschbach, J. Phys. Chem. A, 2009, 113, 4117–4124.
- 71 J. Autschbach, S. Zheng and R. W. Schurko, *Concepts Magn. Reson., Part A*, 2010, **36A**, 84–126.